Inorganic Chemistry

pubs.acs.org/IC
Article

Probing the Local Environment in Potassium Salts and Potassium-Promoted Catalysts by Potassium Valence-to-Core X-ray Emission Spectroscopy

Atanu Rana, Sergey Peredkov, Malte Behrens, and Serena DeBeer*

Cite This: *Inorg. Chem.* 2024, 63, 16217−16223
Read Online

ABSTRACT: Potassium plays an important role in biology as well as a promoter in heterogeneous catalysis. There are, however, limited characterization techniques for potassium available in the literature. This study elucidates the potential of element-selective X-ray emission spectroscopy (XES) for characterizing the coordination environment and the electronic properties of potassium. A series of XES measurements were conducted, primarily focusing on the VtC transition ($K\beta_{2,5}$) of potassium halides (KCl, KBr, and KI) and oxide-bound potassium salts, including potassium nitrate (KNO_3) and potassium carbonate (K_2CO_3). Across the series of potassium halides, the VtC transition energy is observed to increase, as accurately reproduced by TDDFT calculations. Molecular orbital analysis suggests that the $K\beta_{2,5}$ transition is primarily derived from halide *n*p contributions, with the primary factor influencing the energy shift being the metal−ligand distances. For oxide ligands, an additional $K\beta''$ transition appears alongside the $K\beta_{2,5}$, which is attributed to a low-energy ligand *n*s, as elucidated by theoretical calculations. Finally, the XES spectra of two potassium-promoted catalysts for ammonia decomposition/synthesis were measured. These spectra show that potassium within the catalyst is distinct from other K salts in the VtC region, which could be promising for understanding the role of potassium as an electronic promoter.

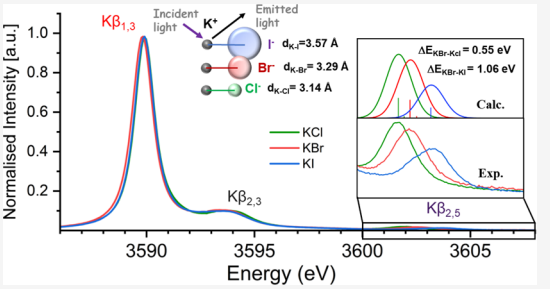

INTRODUCTION

Potassium plays an essential role in countless biological and chemical processes.[1,2] Notable examples include the role of K^+ in regulating ion channels,[3−5] which control a diverse array of cellular processes,[6,7] including the function of neuronal, muscular, and cardiac tissue.[8] In chemistry, potassium serves as an electronic promoter in heterogeneous catalysts, where it is essential for obtaining optimal activity in Fischer−Tropsch, Haber-Bosch catalysts, and reverse water gas shift (RWGS) catalysts.[9−15] Despite the wide range of important processes in which potassium is involved, experimental probes for K ions are relatively limited. K ions are not visible from optical absorption, and the [Ar] electron configuration of the cation also renders it EPR silent. In biology, most of our present understanding of potassium coordination environments has come from protein crystallography.[7,16,17] More recently, developments using magic angle spinning ^{39}K NMR have shown promise as an alternative method for the characterization of the local K environment.[18,19] Further, we note that element-selective probes, such as X-ray absorption (XAS) and XES, should, in principle, provide another means to selectively characterize the changes that occur in the potassium coordination environment. While several reports have been made using potassium extended X-ray absorption fine structure (EXAFS),[21,22] to our knowledge there are only a few previous reports of K XES spectroscopy, and to date, reports have focused only on potassium halides (KCl, KBr, and KI).[20−22] The relative sparsity of both XES (and XAS/EXAFS) studies on K is, in our view, due in large part to the limited number of synchrotron beamlines where such measurements can be carried out.[23−27] Recently, we have designed and commissioned the PINK beamline at BESSY, which is an ideal setup for XES in the tender X-ray regime,[28] thus enabling measurements on potassium and opening up the possibility for K measurements on catalytic systems. Of particular interest in this context are $K\beta$ and valence-to-core (VtC) XES spectra, which have in recent years seen widespread use for a range of first row transition metals due to the now well-established sensitivity to ligand identity and protonation state.[29−38] In contrast, the applications of XES to alkali and alkali earth metals have been very limited,[39,40] and to our knowledge, no applications of K XES to catalytic materials have been previously reported.

Herein, we perform a systematic calibration study on a series of potassium salts in order to establish the information content

Received: May 19, 2024
Revised: August 9, 2024
Accepted: August 13, 2024
Published: August 20, 2024

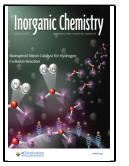

https://doi.org/10.1021/acs.inorgchem.4c02069
Inorg. Chem. 2024, 63, 16217−16223

of Kβ and VtC XES. The sensitivity of the K VtC XES to ligand identity and potassium-ligand distance is established. Our experimental results are correlated to density functional theory (DFT) calculations in order to more quantitatively assess the spectral changes. The potential of K VtC XES for future studies in chemical catalysis is highlighted through application of this method to a potassium-promoted iron ammonia synthesis catalyst.[41,42]

MATERIALS AND METHODS

Sample Preparation. Potassium chloride (KCl), potassium bromide (KBr), potassium iodide (KI), potassium nitrate (KNO_3), and potassium carbonate (K_2CO_3) were purchased from Sigma-Aldrich and used without further purification.

Fe/MgO catalysts were synthesized from $MgFe_2O_4$ precatalysts, which were obtained from Fe/Mg layered double hydroxide (LDH) precursor samples based on a previously reported procedure,[41,42] and promoted by impregnation with KNO_3. The following commercially available chemicals were used without further purification: iron(II) sulfate heptahydrate (≥99.5% p.a., ACS, Carl Roth GmbH & Co. KG), iron(III) nitrate nonahydrate (≥98% p.a., ACS, Alfa Aesar GmbH), and magnesium nitrate hexahydrate (≥98%, ACS, Alfa Aesar GmbH). The precipitation agent was a mixture of sodium carbonate (p.a., AppliChem GmbH) and sodium hydroxide (≥99%, VWR International BVBA). For wet-impregnation, potassium bicarbonate (puriss., Riedel-de Haën) was used without further purification. The synthesis of the LDH phase was conducted through pH-controlled coprecipitation at pH = 10.5 and 50 °C using an automated OptiMax synthesis workstation provided by Mettler Toledo. A solution with a 1:1:1 ratio of Mg^{2+}, Fe^{2+}, and Fe^{3+} and a total metal cation concentration of 0.8 mol/L was codosed with the precipitating agent (0.60 mol/L Na_2CO_3 and 0.09 mol/L NaOH) to keep the pH constant. The precipitate was aged for 1 h in the mother liquid, washed, recovered by centrifugation, and dried at 80 °C to yield the LDH precursor.

The Catalyst_K_1 and Catalyst_K_2 were prepared using two distinct methods, which varied depending on the addition steps of the promoter. In both samples, the mass of KNO_3 was adjusted to yield a K loading of 2 wt %. In the preparation of Catalyst_K_1, KNO_3 was impregnated onto the LDH precursor prior to the calcination step, whereas for Catalyst_K_2, the LDH precursor was first calcined, followed by impregnation of KNO_3 and subsequent recalcination. The calcination process was carried out in a muffle furnace at 600 °C (with a heating rate of 2 K/min) for 2 h. Calcination led to the decomposition of the LDH structure and the formation of a K-promoted $MgFe_2O_4$ spinel. In the unpromoted reference sample[39] as well as in Catalyst_K_2, an α-Fe_2O_3 (hematite) byphase was detected. Subsequent to catalyst preparation, the catalytic activity was tested in both instances.

All samples were finely ground and pressed into pellets. Potassium salts were sealed using 30 μm Kapton tape windows. Samples containing iodide and bromide were additionally shielded with 800 nm Al foil to prevent detector interference from visible light fluorescence. For ammonia synthesis catalysts (Catalyst_K_1 and Catalyst_K_2), 8 μm Kapton tape served as a protective cover. The catalysts were studied in their calcined state. Subsequently, the samples were transferred into the spectrometer's vacuum system and measured at room temperature.

XES Measurements. All potassium Kβ X-ray emission spectroscopy (XES) data were collected at the PINK tender X-ray beamline at BESSY II. The beam size was 30 × 500 μm fwhm ($V \times H$). The excitation energy was 4000 eV, and the incoming photon flux was ~10^{13} ph/s. The fwhm at this excitation energy is 80 eV. The spectra were recorded by the use of a dispersive in vacuum von Hamos spectrometer equipped with a Si(110) cylindrically bent crystal (bending radius R = 250 mm) and a Great Eyes CCD (26 μm × 26 μm pixel size, 256 × 1024 pixels) detector. The Si(220) reflection was utilized at Bragg angles from 62 to 65°. Under these conditions, the spectrometer resolution was about 0.8−1 eV.[28]

Calibration of the energy scale was done by measuring the emission lines of the Sb foil. The energy points used for the energy calibration were Sb Lα1:3604.72 eV and Lα2:3595.32 eV (X-ray data booklet).[43] To define the peak positions, these lines were fitted with split Voigt functions[44] (an asymmetric shape of La1,2 lines is a sum of natural line and instrumental function asymmetries), in which the width of the distribution is different between left and right slopes. Energies were translated into Bragg angles, and a fit with a tangential function was applied.

Computational Details. All calculations were performed using the ORCA program package version 5.0.1.[45] DFT calculations were performed using the BP86[46] functional in the def2-SVP basis set.[47,48] All calculations were carried out using the crystallographically reported coordinates without additional optimization.[49−55] For infinite lattice compounds, calculations were performed by either (1) using a minimum quantum cluster (small QC) comprised of the potassium and its nearest neighbors, a total of 7 atoms, or (2) embedding the larger quantum cluster (large QC), a total of 80 atoms. For larger quantum cluster formation, the "Crystal Prep" technique[56] has been used, which is available in the present version of ORCA. It was determined that the minimum quantum cluster approach more closely agreed with experimental trends as compared to the embedding quantum cluster method. Therefore, calculations utilizing solely the minimum quantum region are the primary focus. Calculated VtC XES spectra are based on the combined electric and magnetic dipole and electric quadrupole contributions.[29,57,58] However, only electric dipole transitions were found to have non-negligible intensities. The calculated energy axis is not an absolute energy axis. To make our comparison more reasonable, the calculated energy axis is shifted by a constant value of 104.4 eV to align with the experimental energy axis. Reported spectra are Gaussian broadened by 2.0 eV. This broadening was chosen in order to obtain the best visual agreement between the calculated and experimental spectra. The broadening accounts for the spectrometer resolution and the K 1s core hole lifetime as well as additional factors such as site heterogeneity and possible charge transfer and/or multielectron excitations, which also contribute to the experimental broadening.

RESULTS AND ANALYSIS

Potassium Halide Salts. Figure 1 (right panel) compares the Kβ mainline for KCl, KBr, and KI. All spectra show a maximum at ~3589.7 eV, which corresponds to a 3p−1s transition (Figure S1). The similar energy for all potassium salts is consistent with the expected similar K description in all compounds. Only the Kβ main line of KBr is ~0.1 eV lower

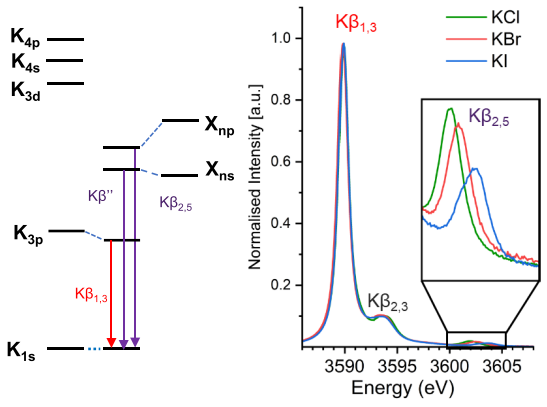

Figure 1. Simplified MO diagram schematically depicting the origin of the transitions in the K Kβ XES spectrum (left) and the experimental XES spectra of KCl, KBr, and KI, with the VtC region enlarged approximately 50-fold in the inset (right). The Kβ XES spectral intensities were normalized to 1.0 at the maximum of the K$\beta_{1,3}$ mainline.

https://doi.org/10.1021/acs.inorgchem.4c02069
Inorg. Chem. 2024, 63, 16217−16223

than others, which might arise due to some ligand-derived contribution to this transition. In addition, all of the potassium salts show a shoulder at ∼3593.8 eV. The 4 eV splitting is clearly too large to be attributed to K 3p spin-orbit splitting and may potentially result from a two-electron process. We note that this feature was also observed in the previously reported Kβ spectrum of potassium halide salts, where it was assigned as a satellite feature resulting from a double ionization event.[25,26] We note that for all five potassium samples measured in this study, the Kβ main line does not vary by more than 0.1 eV (Figure S1). Hence, for the remaining compounds, we focus on the high-energy VtC features, which show clear variations across the series.

Figure 2A depicts the VtC XES images for the potassium halides. Based on analogy to transition-metal VtC XES, the

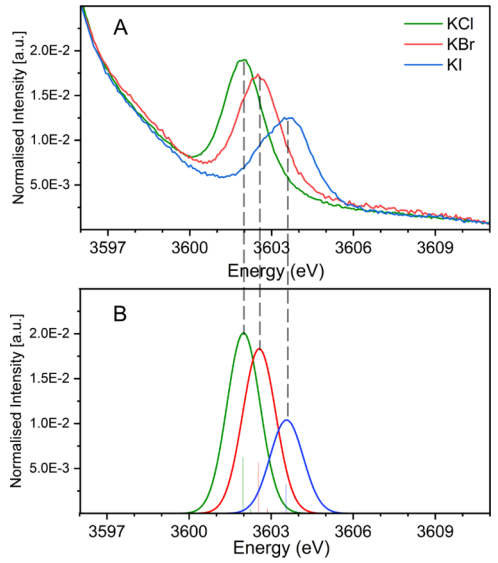

Figure 2. (A) Experimental and (B) calculated spectral comparison of the VtC XES region of KCl, KBr, and KI. The DFT calculated energy axis is shifted by 104.4 eV.

observed features may be attributed to transitions from the filled halide *n*p valence levels to the K 1s core hole (or so-called K$\beta_{2,5}$ features). Ongoing from KCl to KBr to KI, these features shift up in energy by ∼1.6 eV (Table 1). This is

Table 1. Experimental and Calculated Energy of K$\beta_{1,3}$ and K$\beta_{2,5}$ Transitions[a]

electronic transition		KCl	KBr	KI
K$\beta_{1,3}$(eV)	experimental	3589.9	3589.81	3589.91
	calculated	3592.05	3592.05	3592.13
K$\beta_{2,5}$(eV)	experimental	3601.9	3602.5	3603.62
	calculated	3602.00	3602.56	3603.58

[a]The calculated energy axis is shifted 104.4 eV.

consistent with a decrease in the ligand valence ionization energy. We note, however, that the valence ionization energies change by only 0.55 eV on going from Cl^- to I^- and hence the difference in ionization energy is not the only source of the observed shift.[59]

In order to more quantitatively understand the origin of the modulations in energy and intensity of the K$\beta_{2,5}$ features across the halide series, DFT calculations were performed. The calculations were carried out in two different ways: (i) calculating the larger quantum cluster (large QC includes 80 atoms per calculation) and (ii) considering a minimum quantum cluster composed of a $[KX_6]^{5-}$ unit (Figure S2). As shown in Figure 2B, the calculated XES spectra with minimal QC cluster successfully reproduce the relative energy and intensity trends for the K$\beta_{2,5}$ features of all of the halides. We note, however, that in the experimental VtC spectrum for KI and KBr, there is an asymmetry in the K$\beta_{2,5}$ features that is not captured by our calculations. These may arise from the energy differences between the halides (Br^- and I^-) in their $P_{1/2}$ and $P_{3/2}$ states, as established by Gomes and co-worker using relativistic embedded equation of motion coupled cluster theory.[60] However, the level of theory employed in this study is not sufficient to capture such effects. The embedded QC calculations somewhat underestimate the shifts among different complexes. This may suggest that there is too much charge compensation from the lattice (Figure S3C). Given the already good agreement with a minimal quantum cluster, all further analyses have thus been performed considering only the small QC calculations in our study.

The calculated spectra were then analyzed in terms of the transitions shown in Figure 1. The transitions are K$\beta_{1,3}$ (3p to 1s), Kβ'' (ligand *n*s to K 1s), and K$\beta_{2,5}$ (ligand *n*p to 1s) accordingly (Figures S4−S6). We note in the present case, both experimentally and computationally, there is significant overlap between the K$\beta_{1,3}$ and Kβ'' features. Hence the orbital population analysis is given in terms of K 3p, L *n*s, and L *n*p contributions. In the K$\beta_{1,3}$ region, the K 3p character dominates in all cases (>92% for KCl and KI, ∼73% for KBr), while in the K$\beta_{2,5}$ region, ligand p contributions dominate (>92%, Table S2). However, the low-intensity Kβ'' features are not well resolved for the halides, as these appear to largely overlap with the K$\beta_{1,3}$. The orbital analysis shows that the relative energy of the ligand *n*s orbital decreases from I^- to Br^- to Cl^-. The Br^- *n*s orbital has an energy level closest to K 3p, resulting in a higher degree of orbital overlap. Consequently, the Br *n*s character (25%) significantly increases in the K$\beta_{1,3}$ region relative to the other two halides.

The experimental and calculated VtC XES spectra are compared in Figure 2B and show that the trends in both energies and intensities are well reproduced at this level of theory. As ionization energy differences can account for only a portion of the observed shift, additional calculations were performed in order to understand the impact of potassium-halide distance on the VtC energies as well as their intensities. As is expected, the K-halide distance increases across the series going from d_{K-Cl}: 3.14 Å to d_{K-Br}: 3.29 Å to d_{K-I}: 3.53 Å, due to the difference in the ionic radius of the corresponding halides. Therefore, in addition to the intrinsic ionization energy contributions, the K-halide distance may also play a role in the observed K$\beta_{2,5}$ energies and intensities. To systematically test this, calculations were performed by changing the average potassium-halide distances from 3.0 to 3.6 Å with a periodic increment of 0.2 Å.

As shown in Figure 3A,B, the K$\beta_{2,5}$ transition energy increases linearly with increasing K−Cl bond length, while the peak intensity correspondingly decreases. These trends are consistent with the bonding molecular orbital being less stabilized (hence, the higher energy) and having less potassium character (hence, the decreased intensity). A similar trend is also observed for KBr and KI (Figure S7) with a similar distance-dependent energy shift and decrease in intensity upon

https://doi.org/10.1021/acs.inorgchem.4c02069
Inorg. Chem. 2024, 63, 16217−16223

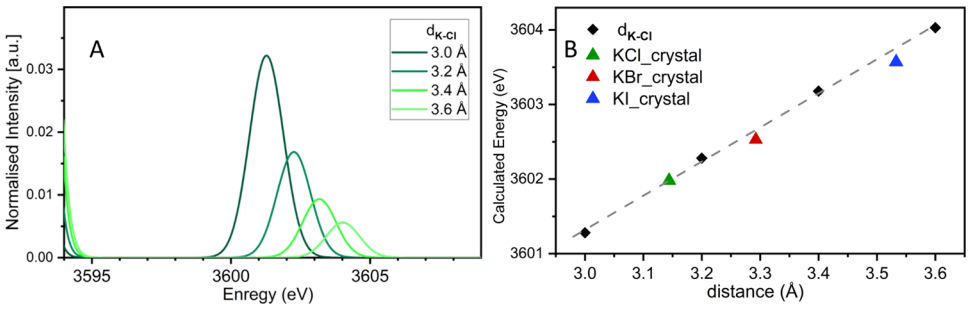

Figure 3. (A) Calculated K VtC XES region for KCl for varying K−Cl distances from 3.0 to 3.6 Å. (B) Correlation of K-halide distances with the $K\beta_{2,5}$ transition energies. The colored triangles correspond to the experimental distances, while the black diamonds correspond to the hypothetical distances from panel A. The DFT calculated energy axis is shifted by 104.4 eV.

elongation of the K−X bond. Figure 3B shows an overlay of the calculated KCl, KBr, and KI $K\beta_{2,5}$ transition energies at the experimental K-halide distances (green, red, and blue triangles for KCl, KBr, and KI, respectively) as compared to the calculated KCl $K\beta_{2,5}$ energies for K−Cl distances from 3.0 to 3.6 Å (black diamonds). The black line is a fit through the points generated from the hypothetical K−Cl series. The comparison plot indicates that the modulations in the energy of the $K\beta_{2,5}$ features across the halide series mainly originate from the inherent metal-ligand bond distances of the corresponding potassium halide. The slight deviations of the KBr and KI from the K−Cl distance-dependent trend line are likely a reflection of the differences in ionization energy of Br and I relative to Cl. These shifts of 0.13 and 0.20 eV for KBr and KI relative to the trend line are in good agreement with the relative changes in the Br and I ionization energies relative to that of Cl (0.25 and 0.55 eV, respectively). It has been observed that the VtC transition intensity decreases ongoing from KCl to KI both in experimental and theoretical calculated results. A similar trend is observed in calculated results when increasing the hypothetical K−X (X = Cl, Br, I) distance. These observations indicate that the K−X distance also plays a significant role in the transition intensity. To further investigate the effect of ligand identity on this transition intensity, we have compared KCl and KBr $K\beta_{2,5}$ intensities at a K−X distance of 3.2 Å, and a significant difference in the intensity ratio was observed (Intensity ratio ($I_{KBr/KCl}$) = 1.39). A noticeable difference for all the halides is the different atomic radii (1.81, 1.96, and 2.2 Å for Cl^-, Br^- and I^-, respectively), an indication of different polarizabilities (3.69, 4.81, and 7.16 $Å^3$ for Cl^-, Br^- and I^-, respectively).[61] The polarizability ratio between Br^- and Cl^- is 1.31, similar to the difference in $K\beta_{2,5}$ intensity ratios, as noted above. These results indicate that the VtC $K\beta_{2,5}$ intensity depends on both the metal-ligand distance and the ligand polarizability.

KNO_3 vs K_2CO_3. Having established trends in the VtC XES energies and intensities for potassium halides, we then extended this approach to oxygen-bound potassium complexes, including K_2CO_3 and KNO_3. The results showed that the $K\beta_{1,3}$ transitions of K_2CO_3 and KNO_3 occur at energies similar to those of the potassium halides, around 3589.7 eV (Figure S1). Figure 4A depicts an overlay plot of the experimental VtC XES region of K_2CO_3 and KNO_3 with KCl, included as a reference halide for comparison. The highest energy VtC feature for K_2CO_3 is at a similar energy to that of KCl (3601.9 eV for K_2CO_3 vs 3601.97 eV for KCl), albeit lower in intensity. Further K_2CO_3 exhibits an additional VtC transition at 3597.43 eV in the region typically referred to as the $K\beta''$

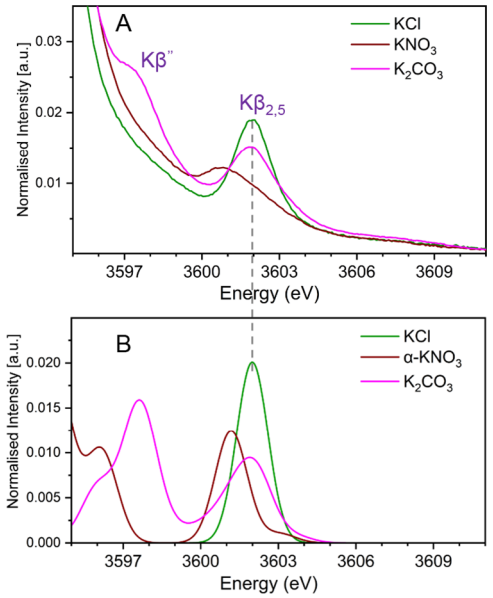

Figure 4. (A) Experimental and (B) calculated spectral comparison of the VtC XES spectra of KCl, KNO_3, and K_2CO_3. The DFT calculated energy axis is shifted by 104.4 eV.

region. In contrast for KNO_3, only a single $K\beta_{2,5}$ transition appears at 3600.79 eV, which is ∼1.1 eV lower than that of KCl and K_2CO_3.

Theoretical calculations were performed to understand these transitions. The experimental XES spectrum was measured using a powder form of potassium salts. However, the crystal structures of potassium salts in theoretical calculations can be a useful starting point for a logical initial guess. For our calculation, the structural coordinates have been taken from the reported crystal structures.[52,54,55]

The K_2CO_3 has two inequivalent potassium coordination sites in its crystal structure. One site is six-coordinated with six monodentate carbonate ligands, while the other is nine-coordinated with five carbonate ligands (one monodentate and four bidentate, Figure S8C). The calculated $K\beta$ X-ray emission spectrum of K_2CO_3 contains both high-energy $K\beta_{2,5}$ and low-energy $K\beta''$ features. This is in good agreement with the experimental observations (Figure 4). The orbital population analysis of the calculated spectrum indicates that the $K\beta''$ transition arises from the hybridization of K 3p orbitals with O 2s valence orbitals. The lower the energy of the $K\beta''$ transition, the greater the contribution from O 2s orbitals. To deconvolute the individual contributions of the two potassium

https://doi.org/10.1021/acs.inorgchem.4c02069
Inorg. Chem. 2024, 63, 16217−16223

coordination sites to the VtC spectrum, two separate calculations have been performed (Figure S9B). The results show that both sites contribute to the K$\beta_{2,5}$ region, but the nine-coordinated site $[K(CO_3)_5]$ dominates the spectral intensity in this energy region. In contrast, the six-coordinated site $[K(CO_3)_6]$ is the dominant contributor in the Kβ'' region (Figure S9). Notably, in the K_2CO_3 crystal structure, the average K−O bond distance of the six-coordinate site is 2.67 Å, and for the nine-coordinate site, it is 2.96 Å. Comparing the coordination-site-specific relative intensities and the average metal-ligand distances, it is clear that shorter K−O distances lead to higher transition intensities.

KNO_3 is known to exist in four crystal phases: α, β, γ, and delta (δ). The α and δ phases are stable at room temperature, while the β and γ phases are metastable.[53] The β and γ phases can be induced by heating or cooling the α phase in a certain temperature range. As the current study was carried out at room temperature, the α and δ phases (Figure S9) were explored for the DFT calculations. The results of these calculations are shown in Figure S10. While both phases show a predicted K$\beta_{2,5}$ transition at ∼3601.2 eV, in both cases, the calculated spectrum is ∼0.4 eV higher in energy relative to the experiment. It is possible that the powder form of the KNO_3 sample introduces some disorder that is not modeled by the DFT calculations of the crystallographic models. We note, however, that the qualitative energy and intensity trends for KNO_3 relative to KCl and K_2CO_3 are reasonably well captured by theory, clearly showing that the K$\beta_{2,5}$ transition of KNO_3 appears to lower energy with decreased intensity.

K-XES Comparison with NH_3 Synthesis/Decomposition Catalyst. Having assigned the K VtC XES spectra for a series of K salts of known composition, we then extended our K VtC XES to potassium-impregnated $MgFe_2O_4$ catalysts utilized in NH_3 synthesis and decomposition reactions.[39,62] In heterogeneous catalysis, small amounts of potassium ions are frequently used as catalytic promoters. In the present case, KNO_3 was used as a potassium source as described in the materials and method section to result in an approximate potassium loading of 2 wt % (2,05% for Catalyst _K_1, 1,76% for Catalyst _K_2 as determined by AAS). Depending upon when the potassium was introduced to the catalysts (before calcination on the LDH precursor or after calcination on the spinel precatalyst), two different types of catalysts have been prepared for our measurements, which are labeled as Catalyst_K_1 and Catalyst_K_2. A similar K$\beta_{1,3}$ transition energy (∼3589.7 eV) is observed for both catalysts relative to the potassium salts (Figure S11), again indicating the presence of a similar potassium electronic state.

Figure 5 depicts an overlay of the VtC XES for the catalysts along with the precursor KNO_3, which shows weak VtC XES features for both catalysts with a lower intensity and a broader energetic spread relative to the KNO_3 reference with a slight shift to higher energy. These data suggest that the state of potassium in catalysts after calcination has changed relative to its conformation in the KNO_3 source material. This can be attributed to the calcination at 600 °C, which triggers the α-to-β phase transition of KNO_3 at approximately 130 °C, the melting of KNO_3 at 334 °C, and the beginning of the thermal decomposition into oxygen and potassium nitrite above 550 °C. These temperatures refer to the bulk compound and may differ from those of highly dispersed materials, which can be obtained by the wetting of the catalyst's pores with a molten salt layer (melt infiltration).[63]

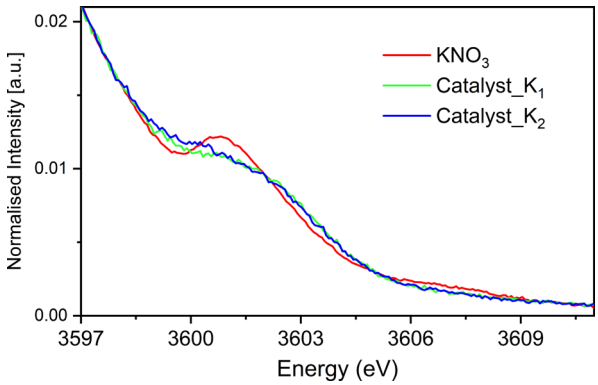

Figure 5. Overlay plot of K$\beta_{2,5}$ transition region of KNO_3 with the NH_3 synthesis catalysts Catalyst_K_1 and Catalyst_K_2.

Utilizing the lessons, we obtained from the investigation of the known salts it appears that the potassium is interacting weakly with the surrounding ligands, manifesting in the shift to higher energy and decrease in intensity. In these catalysts, it is anticipated that potassium will predominantly reside on the surface, exhibiting a high dispersion. Consequently, the interaction between potassium and surrounding ligands is expected to be relatively weaker compared to that of bulk species within a crystal lattice. Our findings are consistent with this observation. This modulation in the potassium, however, is the same in Catalyst_K_1 and Catalyst_K_2, regardless of the stage of potassium impregnation. While at the present state of understanding, we cannot predict the exact coordination site of potassium in the catalysts, these results suggest that if potassium is directly involved as an electronic promoter during catalysis, this spectral region should provide experimentally observable changes. Hence, the present study provides the groundwork for potential future applications in catalysis.

CONCLUSIONS

This work introduces K XES results for various potassium salts and two potassium-promoted catalysts. A progressive energy shift from KCl to KBr to KI is observed in the K$\beta_{2,5}$ VtC XES transition for potassium halides. Theoretical calculations support the conclusion that potassium-halide distances are the primary factors influencing this energy shift in halide salts. Furthermore, it is confirmed that the Kβ'' transitions for all potassium halides are obscured by the intense K$\beta_{1,3}$ transition. In oxygen-ligated complexes such as K_2CO_3, alongside the K$\beta_{2,5}$ transition, an additional Kβ'' transition emerges due to the low-energy contribution from the ligand (O)2s and the short K−O distances, which give rise to increased spectral intensity. The K_2CO_3 crystal structure has two inequivalent potassium coordination sites that give rise to distinct features in the VtC XES. The six-coordinated site, with shorter K−O distances, dominates the Kβ'' region, while the nine-coordinated site dominates the K$\beta_{2,5}$ region. This information can be utilized to understand the electronic structure and bonding interactions in K_2CO_3. For KNO_3, while full quantitative agreement is not achieved, the qualitative trends relative to those of other potassium salts are captured. Finally, K XES spectra of an NH_3 synthesis/decomposition catalyst reveal that the potassium within the catalyst is clearly modulated relative to the KNO_3 precursor in the VtC region and is also distinct from other K salts. Our understanding at present indicates substantial alterations in the coordination

https://doi.org/10.1021/acs.inorgchem.4c02069
Inorg. Chem. 2024, 63, 16217−16223

environment of the precursor postcalcination. However, additional research is imperative to precisely forecast the exact potassium configuration within the catalyst. The results presented here form the foundation for future operando studies of catalysts aimed at elucidating the role of potassium as a promoter.

■ ASSOCIATED CONTENT

Data Availability Statement

All relevant data, including the experimental XES data for all potassium salts, NH_3 decomposition catalysts, and the calculated ORCA files, are available at 10.17617/3.TTWAOX.

Supporting Information

The Supporting Information is available free of charge at https://pubs.acs.org/doi/10.1021/acs.inorgchem.4c02069.

Additional experimental and calculated spectra, as well as transition assignments (PDF)

■ AUTHOR INFORMATION

Corresponding Author

Serena DeBeer − *Max Planck Institute for Chemical Energy Conversion, D-45470 Mülheim an der Ruhr, Germany;* orcid.org/0000-0002-5196-3400; Email: serena.debeer@cec.mpg.de

Authors

Atanu Rana − *Max Planck Institute for Chemical Energy Conversion, D-45470 Mülheim an der Ruhr, Germany;* orcid.org/0000-0002-2397-5869

Sergey Peredkov − *Max Planck Institute for Chemical Energy Conversion, D-45470 Mülheim an der Ruhr, Germany*

Malte Behrens − *Institute of Inorganic Chemistry, Kiel University, 24118 Kiel, Germany;* orcid.org/0000-0003-3407-5011

Complete contact information is available at: https://pubs.acs.org/10.1021/acs.inorgchem.4c02069

Funding

Open access funded by Max Planck Society.

Notes

The authors declare no competing financial interest.

■ ACKNOWLEDGMENTS

The authors acknowledge the Max Planck Society for funding. The authors thank the PINK beamline staff at BESSY for the allocation of beamtime. A.R. acknowledges funding from the Alexander von Humboldt Foundation. The authors would like to thank the Federal Ministry of Education and Research, Germany (Bundesministerium für Bildung und Forschung, BMBF, Hydrogen flagship project: TransHyDE Forschungsverbund AmmoRef (FKZ 03HY203E and FKZ 03HY203A) for funding. A.R. thanks Dimitrios Manganas for helpful discussions regarding the Crystal-Prep orca calculations. Denise Rein is acknowledged for synthesizing the catalyst samples.

■ REFERENCES

(1) Sardans, J.; Peñuelas, J. Potassium: a neglected nutrient in global change. *Glob. Ecol. Biogeogr.* **2015**, *24*, 261−275.

(2) Stone, M. S.; Martyn, L.; Weaver, C. M. Potassium Intake, Bioavailability, Hypertension, and Glucose Control. *Nutrients* **2016**, *8* (7), 444.

(3) Kuang, Q.; Purhonen, P.; Hebert, H. Structure of potassium channels. *Cell. Mol. Life Sci.* **2015**, *72*, 3677−3693.

(4) Mironenko, A.; Zachariae, U.; de Groot, B. L.; Kopec, W. The Persistent Question of Potassium Channel Permeation Mechanisms. *J. Mol. Biol.* **2021**, *433*, No. 167002.

(5) Kilbourn, B. T.; Dunitz, J. D.; Pioda, L. A. R.; Simon, W. Structure of the K+ complex with nonactin, a macrotetrolide antibiotic possessing highly specific K+ transport properties. *J. Mol. Biol.* **1967**, *30*, 559−563.

(6) Clausen, M. J. V.; Poulsen, H. Sodium/Potassium Homeostasis in the Cell. In *Metal Ions in Life Sciences*; Springer: Dordrecht, 2013; Vol. *12*; pp. 41−67.

(7) Zhou, Y.; Morais-Cabral, J. H.; Kaufman, A.; MacKinnon, R. Chemistry of ion coordination and hydration revealed by a K+ channel−Fab complex at 2.0 Å resolution. *Nature* **2001**, *414*, 43−48.

(8) Humphries, E. S. A.; Dart, C. Neuronal and Cardiovascular Potassium Channels as Therapeutic Drug Targets: Promise and Pitfalls. *SLAS Discovery* **2015**, *20*, 1055−1073.

(9) Second, C. R.; Edition, E.; Ertl, G.; Knözinger, H.; Schüth, F.; Weitkamp, J. *KGaA, Handbook of heterogeneous catalysis*; Wiley-VCH: Weinheim, Germany, 2008.

(10) Huo, C.-F.; Wu, B.-S.; Gao, P.; Yang, Y.; Li, Y.-W.; Jiao, H. The Mechanism of Potassium Promoter: Enhancing the Stability of Active Surfaces. *Angew. Chem., Int. Ed.* **2011**, *50*, 7403−7406.

(11) Lin, B.; Wei, K.; Ma, X.; Lin, J.; Ni, J. Study of potassium promoter effect for Ru/AC catalysts for ammonia synthesis. *Catal. Sci. Technol.* **2013**, *3*, 1367−1374.

(12) Jedynak, A.; Kowalczyk, Z.; Szmigiel, D.; Raróg, W.; Zieliński, J. Ammonia decomposition over the carbon-based iron catalyst promoted with potassium. *Appl. Catal., A* **2002**, *237*, 223−226.

(13) Ertl, G.; Prigge, D.; Schloegl, R.; Weiss, M. Surface characterization of ammonia synthesis catalysts. *J. Catal.* **1983**, *79*, 359−377.

(14) Loiland, J. A.; Wulfers, M. J.; Marinkovic, N. S.; Lobo, R. F. Fe/γ-Al2O3 and Fe−K/γ-Al2O3 as reverse water-gas shift catalysts. *Catal. Sci. Technol.* **2016**, *6*, 5267−5279.

(15) Wang, Y.-X.; Wang, G.-C. A Systematic Theoretical Study of Water Gas Shift Reaction on Cu(111) and Cu(110): Potassium Effect. *ACS Catal.* **2019**, *9*, 2261−2274.

(16) Coates, L. Ion permeation in potassium ion channels. *Acta Crystallogr. D* **2020**, *76*, 326−331.

(17) Doyle, D. A.; Cabral, J. M.; Pfuetzner, R. A.; Kuo, A.; Gulbis, J. M.; Cohen, S. L.; Chait, B. T.; MacKinnon, R. The Structure of the Potassium Channel: Molecular Basis of K+ Conduction and Selectivity. *Science* **1998**, *280*, 69−77.

(18) Moudrakovski, I. L.; Ripmeester, J. A. 39K NMR of Solid Potassium Salts at 21 T: Effect of Quadrupolar and Chemical Shift Tensors. *J. Phys. Chem. B* **2007**, *111*, 491−495.

(19) Wu, G.; Gan, Z.; Kwan, I. C. M.; Fettinger, J. C.; Davis, J. T. High-Resolution 39K NMR Spectroscopy of Bio-organic Solids. *J. Am. Chem. Soc.* **2011**, *133*, 19570−19573.

(20) Chikara Sugiura, C. S.; Hiroyuki Yamasaki, H. Y. X-Ray Spectroscopic Studies of Potassium Halides. *Jpn. J. Appl. Phys.* **1993**, *32*, 1135.

(21) Parratt, L. G.; Jossem, E. L. X-Ray Spectroscopy of the Solid State: Potassium Chloride. *Phys. Rev.* **1955**, *97*, 916−926.

(22) Miyano, K. E.; Ma, Y.; Southworth, S. H.; Cowan, P. L.; Karlin, B. A. Resonant Raman scattering in potassium and chlorine K_β X-ray emission from KCl. *Phys. Rev. B* **1996**, *54*, 12022−12028.

(23) Kavčič, M.; Žitnik, M.; Bučar, K.; Mihelič, A.; Štuhec, M.; Szlachetko, J.; Cao, W.; Alonso Mori, R.; Glatzel, P. Separation of Two-Electron Photoexcited Atomic Processes near the Inner-Shell Threshold. *Phys. Rev. Lett.* **2009**, *102*, No. 143001.

(24) Davies, C. J.; Mayer, A.; Gabb, J.; Walls, J. M.; Degirmenci, V.; Thompson, P. B. J.; Cibin, G.; Golunski, S.; Kondrat, S. A. Operando potassium K-edge X-ray absorption spectroscopy: investigating potassium catalysts during soot oxidation. *Phys. Chem. Chem. Phys.* **2020**, *22*, 18976−18988.

(25) Deslattes, R. D. *Kβ* Emission Spectra of Argon and KCl. *I. Phys. Rev.* **1964**, *133*, A390−A398.
(26) Deslattes, R. D. *Kβ* Spectra of Argon and KCl. II. Satellite Excitation. *Phys. Rev.* **1964**, *133*, A399−A407.
(27) Glezakou, V.-A.; Chen, Y.; Fulton, J. L.; Schenter, G. K.; Dang, L. X. Electronic structure, statistical mechanical simulations, and EXAFS spectroscopy of aqueous potassium. *Theor. Chem. Acc.* **2006**, *115*, 86−99.
(28) Peredkov, S.; Pereira, N.; Grötzsch, D.; Hendel, S.; Wallacher, D.; DeBeer, S. PINK: a tender X-ray beamline for X-ray emission spectroscopy. *J. Synchrotron Radiat.* **2024**, *31*, 622−634.
(29) Lee, N.; Petrenko, T.; Bergmann, U.; Neese, F.; DeBeer, S. Probing Valence Orbital Composition with Iron K*β* X-ray Emission Spectroscopy. *J. Am. Chem. Soc.* **2010**, *132*, 9715−9727.
(30) Beckwith, M. A.; Roemelt, M.; Collomb, M.-N.; DuBoc, C.; Weng, T.-C.; Bergmann, U.; Glatzel, P.; Neese, F.; DeBeer, S. Manganese K*β* X-ray Emission Spectroscopy As a Probe of Metal−Ligand Interactions. *Inorg. Chem.* **2011**, *50*, 8397−8409.
(31) Pollock, C. J.; DeBeer, S. Insights into the Geometric and Electronic Structure of Transition Metal Centers from Valence-to-Core X-ray Emission Spectroscopy. *Acc. Chem. Res.* **2015**, *48*, 2967−2975.
(32) Lassalle-Kaiser, B.; Boron, T. T., III; Krewald, V.; Kern, J.; Beckwith, M. A.; Delgado-Jaime, M. U.; Schroeder, H.; Alonso-Mori, R.; Nordlund, D.; Weng, T.-C.; Sokaras, D.; Neese, F.; Bergmann, U.; Yachandra, V. K.; DeBeer, S.; Pecoraro, V. L.; Yano, J. Experimental and Computational X-ray Emission Spectroscopy as a Direct Probe of Protonation States in Oxo-Bridged MnIV Dimers Relevant to Redox-Active Metalloproteins. *Inorg. Chem.* **2013**, *52*, 12915−12922.
(33) Cutsail, G. E., III; DeBeer, S. Challenges and Opportunities for Applications of Advanced X-ray Spectroscopy in Catalysis Research. *ACS Catal.* **2022**, *12*, 5864−5886.
(34) Lancaster, K. M.; Roemelt, M.; Ettenhuber, P.; Hu, Y.; Ribbe, M. W.; Neese, F.; Bergmann, U.; DeBeer, S. X-ray Emission Spectroscopy Evidences a Central Carbon in the Nitrogenase Iron-Molybdenum Cofactor. *Science* **2011**, *334*, 974−977.
(35) Rees, J. A.; Martin-Diaconescu, V.; Kovacs, J. A.; DeBeer, S. X-ray Absorption and Emission Study of Dioxygen Activation by a Small-Molecule Manganese Complex. *Inorg. Chem.* **2015**, *54*, 6410−6422.
(36) Pollock, C. J.; Delgado-Jaime, M. U.; Atanasov, M.; Neese, F.; DeBeer, S. K*β* Mainline X-ray Emission Spectroscopy as an Experimental Probe of Metal−Ligand Covalency. *J. Am. Chem. Soc.* **2014**, *136*, 9453−9463.
(37) Pollock, C. J.; Grubel, K.; Holland, P. L.; DeBeer, S. Experimentally Quantifying Small-Molecule Bond Activation Using Valence-to-Core X-ray Emission Spectroscopy. *J. Am. Chem. Soc.* **2013**, *135*, 11803−11808.
(38) Pollock, C. J.; Tan, L. L.; Zhang, W.; Lancaster, K. M.; Lee, S. C.; DeBeer, S. Light-Atom Influences on the Electronic Structures of Iron−Sulfur Clusters. *Inorg. Chem.* **2014**, *53*, 2591−2597.
(39) Mathe, Z.; Pantazis, D. A.; Lee, H. B.; Gnewkow, R.; Van Kuiken, B. E.; Agapie, T.; DeBeer, S. Calcium Valence-to-Core X-ray Emission Spectroscopy: A Sensitive Probe of Oxo Protonation in Structural Models of the Oxygen-Evolving Complex. *Inorg. Chem.* **2019**, *58*, 16292−16301.
(40) Mathe, Z.; McCubbin Stepanic, O.; Peredkov, S.; DeBeer, S. Phosphorus K*β* X-ray emission spectroscopy detects non-covalent interactions of phosphate biomolecules in situ. *Chem. Sci.* **2021**, *12*, 7888−7901.
(41) Folke, J. M. *Reactivity studies in ammonia synthesis*; Doctoral dissertation; Ruhr-University Bochum: Bochum, 2022.
(42) Ortega, K. F.; Rein, D.; Lüttmann, C.; Heese, J.; Özcan, F.; Heidelmann, M.; Folke, J.; Kähler, K.; Schlögl, R.; Behrens, M. Ammonia Decomposition and Synthesis over Multinary Magnesio-ferrites: Promotional Effect of Ga on Fe Catalysts for the Decomposition Reaction. *ChemCatChem.* **2017**, *9*, 659−671.
(43) Thompson, A. C. *X-ray Data Booklet*; Lawrence Berkeley National Laboratory, University of California, 2009.
(44) Hölzer, G.; Fritsch, M.; Deutsch, M.; Härtwig, J.; Förster, E. K-alpha and K-Beta-1,3 x-ray emission lines of the 3d transition metals. *Phys. Rev. A* **1997**, *56*, 4554−4568.
(45) Neese, F. Software update: The ORCA program system—Version 5.0. *WIREs Comput. Mol. Sci.* **2022**, *12*, No. e1606.
(46) Becke, A. D. Density-functional exchange-energy approximation with correct asymptotic behavior. *Phys. Rev. A* **1988**, *38*, 3098−3100.
(47) Weigend, F.; Ahlrichs, R. Balanced basis sets of split valence, triple zeta valence and quadruple zeta valence quality for H to Rn: Design and assessment of accuracy. *Phys. Chem. Chem. Phys.* **2005**, *7*, 3297−3305.
(48) Martin, F.; Zipse, H. Charge distribution in the water molecule—A comparison of methods. *J. Comput. Chem.* **2005**, *26*, 97−105.
(49) Zhang, H.; Jiang, W.; Yang, J.; Liu, Y.-Y.; Song, S.; Ma, J.-F. Four coordination polymers constructed by a novel octacarboxylate functionalized calix[4]arene ligand: syntheses, structures, and photoluminescence property. *CrystEngComm* **2014**, *16*, 9939−9946.
(50) Ott, H. XI. Die Strukturen von MnO, MnS, AgF, NiS, SnJ4, SrCl2, BaF2; Präzisionsmessungen einiger Alkalihalogenide. *Z. Kristallogr. -Crystall. Mater.* **1926**, *63*, 222−230.
(51) Wyckoff, R. W. G. *Crystal Structures*; 2nd ed.; Interscience Publishers New York: New York, 1963; Vol. *1*, p. 467s.
(52) Adiwidjaja, G.; Pohl, D. Superstructure of [alpha]-phase potassium nitrate. *Acta Crystallogr. C* **2003**, *59*, i139−i140.
(53) Nimmo, J. K.; Lucas, B. W. The crystal structures of *γ*- and *β*-KNO3 and the $\alpha < -\gamma < -\beta$ phase transformations. *Acta Crystallogr. B* **1976**, *32*, 1968−1971.
(54) Wolf, S.; Alam, N.; Feldmann, C. *δ*-KNO3: Synthesis and Structure of a New Modification of Potassium Nitrate. *Zeitschrift für anorganische und allgemeine Chemie* **2015**, *641*, 383−387.
(55) Gatehouse, B. M.; Lloyd, D. J. Crystal structure of anhydrous potassium carbonate. *Dalton Trans.* **1973**, 70−72.
(56) Dittmer, A.; Stoychev, G. L.; Maganas, D.; Auer, A. A.; Neese, F. Computation of NMR Shielding Constants for Solids Using an Embedded Cluster Approach with DFT, Double-Hybrid DFT, and MP2. *J. Chem. Theory Comput.* **2020**, *16*, 6950−6967.
(57) Maganas, D.; DeBeer, S.; Neese, F. A Restricted Open Configuration Interaction with Singles Method To Calculate Valence-to-Core Resonant X-ray Emission Spectra: A Case Study. *Inorg. Chem.* **2017**, *56*, 11819−11836.
(58) Rees, J. A.; Wandzilak, A.; Maganas, D.; Wurster, N. I. C.; Hugenbruch, S.; Kowalska, J. K.; Pollock, C. J.; Lima, F. A.; Finkelstein, K. D.; DeBeer, S. Experimental and theoretical correlations between vanadium K-edge X-ray absorption and K*β* emission spectra. *J. Biol. Inorg. Chem.* **2016**, *21*, 793−805.
(59) Holbrook, J. B.; Sabry-Grant, R.; Smith, B. C.; Tandel, T. V. Lattice enthalpies of ionic halides, hydrides, oxides, and sulfides: Second-electron affinities of atomic oxygen and sulfur. *J. Chem. Educ.* **1990**, *67*, 304.
(60) Bouchafra, Y.; Shee, A.; Réal, F.; Vallet, V.; Gomes Severo Pereira, A. Predictive Simulations of Ionization Energies of Solvated Halide Ions with Relativistic Embedded Equation of Motion Coupled Cluster Theory. *Phys. Rev. Lett.* **2018**, *121*, No. 266001.
(61) Pauling, L. C.; Sommerfeld, A. J. W. The theoretical prediction of the physical properties of many electron atoms and ions. Mole refraction, diamagnetic susceptibility, and extension in space. *Proc. R. Soc. Lond. Ser. A Math. Phys. Eng. Sci.* **1927**, *114*, 181−211.
(62) Chen, S.; Jelic, J.; Rein, D.; Najafishirtari, S.; Schmidt, F.-P.; Girgsdies, F.; Kang, L.; Wandzilak, A.; Rabe, A.; Doronkin, D. E.; Wang, J.; Friedel Ortega, K.; DeBeer, S.; Grunwaldt, J.-D.; Schlögl, R.; Lunkenbein, T.; Studt, F.; Behrens, M. Highly loaded bimetallic iron-cobalt catalysts for hydrogen release from ammonia. *Nat. Commun.* **2024**, *15*, 871.
(63) Munnik, P.; de Jongh, P. E.; de Jong, K. P. Recent Developments in the Synthesis of Supported Catalysts. *Chem. Rev.* **2015**, *115*, 6687−6718.

https://doi.org/10.1021/acs.inorgchem.4c02069
Inorg. Chem. 2024, 63, 16217−16223